Interfacial Thermal Fluctuations Stabilize Bulk Nanobubbles

Yuyu Chen,[1,*] Yue Hu,[1] Benlong Wang,[1,2] Xuesen Chu,[3,4] and Lu-Wen Zhang[1,2,†]
[1]Department of Engineering Mechanics, School of Ocean and Civil Engineering, Shanghai Jiao Tong University, Shanghai 200240, China
[2]Key Laboratory of Hydrodynamics (Ministry of Education), School of Ocean and Civil Engineering, Shanghai Jiao Tong University, Shanghai 200240, China
[3]Taihu Lake Laboratory of Deep Sea Technology and Science, Wuxi 214082, China
[4]China Ship Scientific Research Center, Wuxi 214082, China

(Received 28 November 2023; accepted 17 July 2024; published 6 September 2024)

Consensus on bulk nanobubble stability remains elusive, despite accepted indirect evidence for longevity. We develop a nanobubble evolution model by incorporating thermal capillary wave theory that reveals that dense nanobubbles generated by acoustic cavitation tend to shrink and intensify interfacial thermal fluctuations; this significantly reduces surface tension to neutralize enhanced Laplace pressure, and secures their stabilization at a finite size. A stability criterion emerges: thermal fluctuation intensity scales superlinearly with curvature: $\sqrt{\langle h^2 \rangle} \propto (1/R)^n$, $n > 1$. The model prolongs the time frame for nanobubble contraction to 2 orders of magnitude beyond classical theory estimates, and captures the equilibrium radius (90–215 nm) within the experimental range.

DOI: 10.1103/PhysRevLett.133.104001

Bulk nanobubbles exhibit ultralong lifetimes [1,2] challenging the "Laplace pressure bubble catastrophe" predicted by classical bubble physics, i.e., an unmitigated acceleration of bubble shrinkage due to the pressure differential across the interface [3], even in oversaturated conditions [4]. Several key small-scale mechanisms on curved liquid surfaces have been realized to underpin the stability of bulk nanobubbles. Electrostatic stabilization, arising from the nanobubble interface's double-layer structure [5] and modulated by pH [6] and salt [7], appears insufficient to counterbalance even 1% of the Laplace pressure [8]; the origin and enrichment of these surface charges remain puzzling. An alternative presents bulk nanobubbles as surface nanobubbles attached to solid impurities [9,10], accounting for the decrease in surface tension of nanobubble solutions [11,12], but not generalizable to impurity-free systems. Moreover, a diffusion boundary layer [13] or bubble clustering [14] might impede interfacial mass transfer, but relying exclusively on this explanation implies an unrealistic reduction of the diffusion coefficient D by at least 7 orders of magnitude (bubble lifetime $\tau_{\text{life}} \propto 1/D$) [4]. These explanations, while attempting to reconcile observation and theory, fall short, signaling the need for a deeper investigation into the atomic-scale dynamics at the nanobubble interface.

Thermal capillary waves (TCWs) [15] are the thermal fluctuations at the gas-liquid interface resulting from the balance between molecular thermal motion and intermolecular cohesion (surface tension), where gravitational and hydrodynamic effects are negligible at this scale (generally < 1 nm). The mean-square amplitude of TCWs, $\langle h^2 \rangle$, is solely related to the surface tension γ, expressed as [16]

$$\langle h^2 \rangle = \frac{k_B T}{2\pi\gamma} \ln \frac{\lambda_{\max}}{\lambda_{\min}}, \tag{1}$$

where T is the absolute temperature, the Boltzmann constant $k_B = 1.38 \times 10^{-23}$ J/K, $\lambda_{\max}$ and $\lambda_{\min}$ are the longest and shortest wavelengths at the interface, respectively. Vigorous TCWs can account for the extremely low surface tension, supported by direct optical observations [17,18] and molecular dynamics (MD) simulations [19–21]. Notably, nanobubble stability benefits from reduced surface tension; for instance, nanobubbles modified with polarizable surfactants have demonstrated extended lifetimes [22,23]. Having been successfully applied to elucidate the coalescence of nanodroplets [24] and the rupture of nano jets [25,26], TCWs thus emerge as an interfacial property warranting detailed exploration in the context of nanobubbles. However, current constraints in experiments persist at the scale of thermal fluctuation, i.e., subnanometer regime, signifying a pronounced need for expanded theoretical exploration.

In this Letter, we reproduce the entire process of nanobubbles evolving from gas aggregation to stabilization in a homogeneous multiphase medium. By correlating this progression with quantifiable interfacial thermal fluctuations, we provide a robust explanation for the mechanical

*Contact author: yuyuchen@sjtu.edu.cn
†Contact author: lwzhang@sjtu.edu.cn

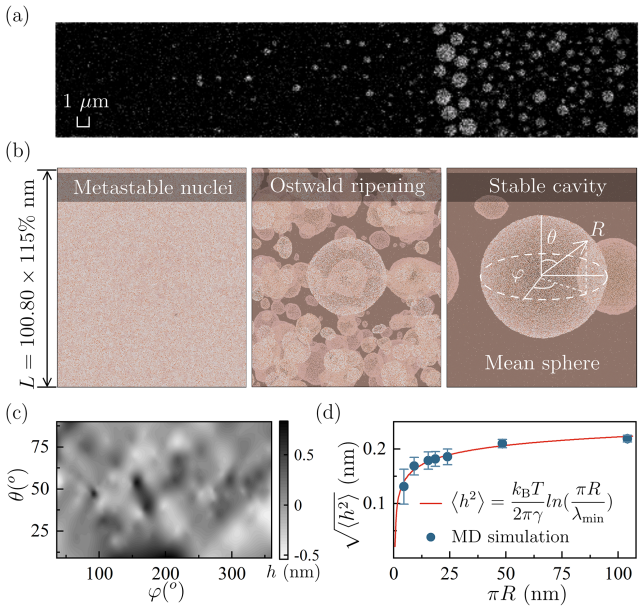

FIG. 1. Initiation of cavitation and calibration of the TCW theory. (a) The very first frame from a video sequence (see SM) of nanobubble solution (2.14×10^8 bubbles/mL) during *in situ* SEM imaging (GeminiSEM, Zeiss, Germany). (b) Typical stages of nanocavity generated from a cubic TIP4P/2005 box in 100.80^3 nm^3. Refer to SM for the full-motion video. (c) Distribution of TCW h over half a spherical cavity, represented in the space spanned by polar angle θ and azimuthal angle φ. (d) Determining $\lambda_{\min} = 0.6$ nm at $T = 300$ K, $\gamma = 0.0684$ N/m within the TCW theory. The theoretical $\sqrt{\langle h^2 \rangle}$ from Eq. (1) (red line) agrees well with that from seven independence atomistic simulations ($R = 1.45$, 2.91, 4.91, 5.90, 7.63, 15.44, and 33.14 nm).

and diffusive equilibrium of nanobubbles, and establish a stability criterion.

Prior to the theoretical exploration, we detected and observed the cavitation process within nanobubble solutions by *in situ* scanning electron microscopy (SEM) equipped with a well-designed liquid nanolab (detailed in Supplemental Material (SM) [27]; see also [29–42] therein). It yields novel, direct evidence for the existence of bulk nanobubbles (cavitation nuclei [43,44]), with the size distribution peaking at around 100 nm (see SM). Notably, the nanoscale cavitation nuclei initially present an irregular spherical profile [see Fig. 1(a)], prompting a focused examination of the thermodynamics at their interfaces.

To delineate TCWs on the evolved nanobubble's interface, we trigger cavitation by applying a negative pressure upon the TIP4P/2005 [45] water box in the large-scale MD simulations, up to 100.80^3 nm^3 (92.87×10^6 atoms), then calibrates characteristic quantities the two characteristic wavelengths $\lambda_{\max}$ and $\lambda_{\min}$ involved in TCWs. Our largest simulation scale of around 100 nm is comparable to nanobubbles detected by SEM. Figure 1(b) illustrates the nucleation process: metastable nuclei progressively coalesce into a nanocavity with internal vacuum, driven by the Ostwald ripening effect.

Now consider the ripening nanocavity as a sphere with mean radius R over which thermal capillary wave fluctuations h superimposed. Figure 1(c) presents a contour map of h depicted in spherical coordinates. The root mean square (rms) amplitude of fluctuation, $\sqrt{\langle h^2 \rangle}$, is determined by spatial interpolation of the interfacial water molecules (detailed in SM). In our simulations $R \sim 10\sqrt{\langle h^2 \rangle}$, the nanocavity's surface is thus approximated as quasiflat relative to the scale of wavelength, permitting the application of TCW theory [24]. In Eq. (1), $\lambda_{\max} = \pi R$ can be adopted since it is proportional to the system's finite dimensions [15]. We then calibrate $\lambda_{\min} = 0.6$ nm by correlating the rms of thermal fluctuation with MD simulations across various nanocavity sizes in a range from 2.90 to 66.28 nm, as shown in Fig. 1(d). Notably, for $\lambda_{\min}$ determination, we assume a constant surface tension $\gamma = 68.4$ mN/m at 300 K [46], overlooking size effect, justified by the alignment of nanocavity dynamics with the well-established Rayleigh-Plesset model for macroscale (see SM). This calibration of TCW theory in nanocavities enables direct quantification of strongly size-dependent surface tension of nanobubble via molecular-scale information.

To explore the correlation between TCW and the mechanical equilibrium at the interface, which serves as a prerequisite for nanobubble stabilization, we derive a TCW-based Young-Laplace equation, incorporating surface tension γ from Eq. (1),

$$\Delta P = \frac{2\gamma}{R} = \frac{k_B T}{\pi R \langle h^2 \rangle} \ln\left(\frac{\pi R}{\lambda_{\min}}\right). \tag{2}$$

$\lambda_{\min} = 0.6$ nm is fixed as it only fluctuates with the types of interfacial molecules. As a verification of Eq. (2), a dense nanobubble is simulated in a supersaturated aqueous system. A unidirectional trapezoidal mechanical wave was applied to approximate a single-frequency acoustic wave $\epsilon = 0.5\epsilon_0[\sin(2\pi t/\tau) + 1]$, where the maximum strain $\epsilon_0 = 0.15$ and the period $\tau = 440$ ps [the top plot of Fig. 2(a), detailed in SM]. A stable dense nanobubble forms after $N_L = 20$ loading cycles. Our simulation of the initial supplemental oxygen (2000 molecules for a nanobubble of $R_0 = 4.90$ nm) and the pressure oscillation aim at accelerating the gas enrichment within the nanobubbles to reflect the rectified diffusion in acoustic cavitation [47]. While heightened local saturation level is posited as a potential requisite for the persistence of nanobubble [48,49], it does not detract from the physical underpinnings of this stability. This is because supersaturation decelerates gas diffusion, but is not capable of altering the inevitable "Laplace pressure bubble catastrophe".

Figure 2(a) shows the remarkably consistency between the Laplace pressure as predicted by the TWC-based Young-Laplace model and the results derived from direct atomic simulations under cyclic loading. Overall, nanobubbles attain a state of relatively stable equilibrium after sufficient oscillations ($N_L > 15$). Interestingly, Eq. (2) achieves strong agreement with experiments [50] and

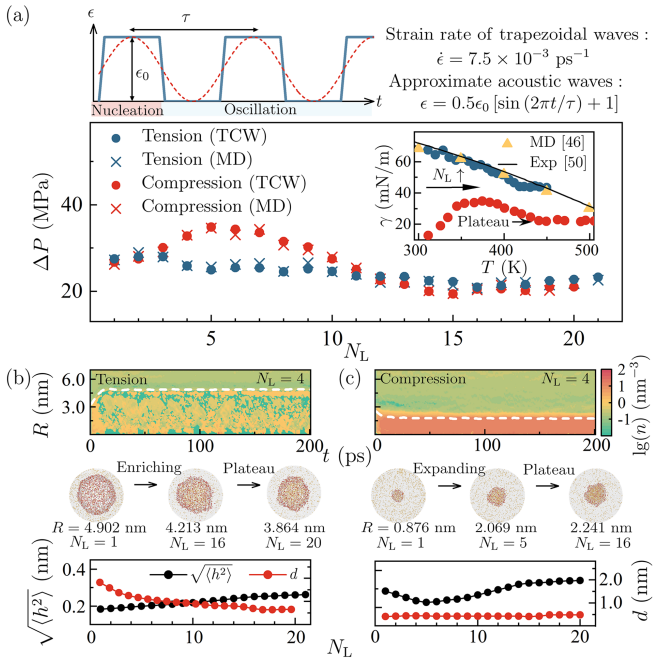

FIG. 2. Mechanical equilibrium of a bulk nanobubble. (a) Laplace pressure undergoes alterations through 20 cycles of tension (blue) and compression (red) loading during the nucleation of a nanobubble. Top inset shows the applied unidirectional tension-compression alternating trapezoidal wave. The right inset shows the temperature dependent curve of the surface tension during oscillations. (b),(c) Molecular-scale features of nanobubbles under tension (b) and compression (c). The contour plot shows the lg(n) distribution (n is number density of the oxygen) at different radial positions R and relaxation times t for $N_L = 4$. The bottom panel shows the rms amplitude $\sqrt{\langle h^2 \rangle}$, the mean molecular spacing d, and the snapshots of nanobubbles under different loading states.

available MD results [46] on the $\gamma - T$ dependency where $N_L \leq 15$ under tensile conditions [inset of Fig. 2(a)]. Thus, the TCW-based model provides a unified depiction of mechanical equilibrium for near-spherical bubbles across both macro and micro scales under negative compression. In contrast, when subjected to compressive stress, γ deviates completely from the macroscopic case, remaining at a low level (10–45 mN/m). At the stage of stable equilibrium achieved adequate pressure oscillations ($N_L > 15$), the Laplace pressure stabilizes at ~22 MPa, and the surface tension becomes insensitive to temperature.

To elucidate how nanobubbles gradually reach equilibrium, we delve into the gas state inside the bubble against both negative and positive pressure environments [Figs. 2(b) and 2(c)]. The synergistic effect of tensile and compressive stresses promotes a remarkable gas enrichment mechanism within the bubble, resulting in a distinct concentration distribution along the radial direction. This is clearly evident during a typical loading cycle ($N_L = 4$), as depicted in the number density contour plots. Here, the mean molecular spacing $d = \sqrt[3]{v}$ (v is the mean molecular volume) is used to estimate the gas density inside the bubble, determined from data sampled between 100 to 200 ps after each loading for robust statistical representation.

Under tension [Fig. 2(b)], d contracts from 1.185 to 0.65 nm. Negative pressure, while expanding the bubble's mass transfer area and promoting gas uptake, leads to an absorption-driven density rise, surpassing volumetric expansion. $\sqrt{\langle h^2 \rangle}$ grows from 0.18 to 0.26 nm, dominated by the thermal activity ($N_L \leq 15$). Conversely, under compression [Fig. 2(c)], d stabilizes at 0.49 nm, indicating persistent high-density states within the nanobubble. In this scenario, $\sqrt{\langle h^2 \rangle}$ is enhanced from 0.23 to 0.34 nm by the strong repulsion among the contracting interfacial molecules and the internal gas clusters, and stabilizes at 0.34 nm underpinned by the enrichment mechanism. These magnified thermal fluctuations diminish surface tension, thereby regulating the mechanical equilibrium of the interface. The consistent $\sqrt{\langle h^2 \rangle}$ after $N_L > 15$ implies that nanobubbles can attain a stable dense state following sustained oscillatory loading. Accordingly, we ascertain two stable equilibrium conditions when the external load is within compressive strength limit: (i) internal gas reaching critical mean molecular spacing $d \sim 0.49$ nm and (ii) the rms of thermal fluctuation maximizing at $\sqrt{\langle h^2 \rangle} \sim 0.34$ nm.

We then advance our understanding of the diffusion dynamics of bulk nanobubbles influenced by TCWs, building on their pivotal role in propelling nanobubbles toward static equilibrium: amplification of $\sqrt{\langle h^2 \rangle}$ during dense nanobubble contraction reduces surface tension γ. According to the Epstein-Plesset (EP) model [51], the diffusion dynamics of a spherical bubble is described as

$$\frac{\mathrm{d}R}{\mathrm{d}t} = -\frac{D\Delta c}{\rho}\left(\frac{1}{R} + \frac{1}{\sqrt{\pi D t}}\right), \tag{3}$$

where $\Delta c = c_b - c_\infty$ denotes the discrepancy in gas concentration adjacent to the bubble (c_b) and in the bulk field (c_∞). Assuming that the solution near the bubble is saturated at the corresponding local pressure, and applying Henry's law $c_b = P_b/k_H = (P_\infty + 2\gamma/R)/k_H$ (P_b is the bubble pressure, P_∞ is the atmospheric pressure, k_H is the Henry constant), we obtain $\Delta c = c_s(2\gamma/RP_\infty - \zeta)$, with $c_s = P_\infty/k_H$ symbolizing the saturation concentration and $\zeta = c_\infty/c_s - 1$ the supersaturation.

According to Eq. (3), the inherent instability of spherical bubbles become evident upon the introduction of any perturbation ΔR to the equilibrium radius R_e (where $\mathrm{d}R/\mathrm{d}t = 0$). A deviation in radius to $R = R_e + \Delta R$ alters the interfacial velocity $\mathrm{d}R/\mathrm{d}t$ by affecting Δc. This alteration implies a self-reinforcing process: contraction ($\Delta R < 0$) accelerates collapse, while expansion ($\Delta R > 0$) favors growth, at arbitrary supersaturation level.

In contrast, we reconsider the diffusion equilibrium of nanobubbles, incorporating the effect of interfacial thermal

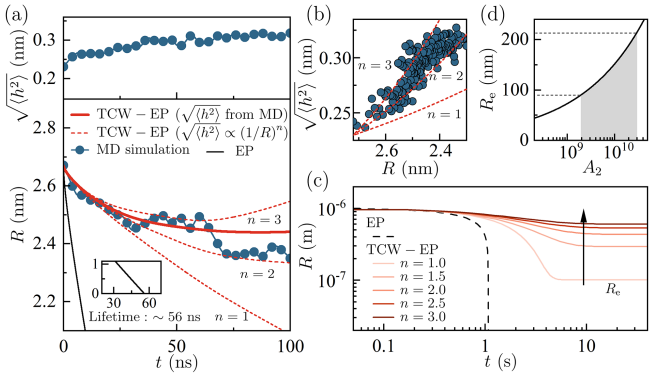

FIG. 3. Long-term stability of nanobubbles. (a) Evolution of the rms of thermal fluctuation $\sqrt{\langle h^2\rangle}$ (top) and the bubble radius R (bottom) obtained from TCW-EP models and MD. $D = 1.0 \times 10^{-9}$ m^2/s, $c_s = 0.091$ kg/m^3 are obtained from MD. (b) Negative correlation between $\sqrt{\langle h^2\rangle}$ and R. (c) Evolution of R from EP and TCW-EP models with varied n adopting $R_0 = 10^{-6}$ m, $\zeta = 0.1$, $T = 300$ K, $P_\infty = 1$ atm, $\sqrt{\langle h_0^2\rangle} = 0.287$ nm, $D = 2.3 \times 10^{-9}$ m^2/s, and $c_s = 0.01$ kg/m^3. (d) The equilibrium radius R_e versus initial dimensionless parameter A_n ($n = 2$) from Eq. (5). The shaded area shows the nanobubble size distribution under typical physical conditions.

motion. A TCW-based EP model recalibrates the γ in Δc as a function of $\langle h^2\rangle$, yielding

$$\frac{dR}{dt} = -\frac{Dc_s}{\rho}\left(\frac{k_B T}{P_\infty R\pi\langle h^2\rangle}\ln\frac{\pi R}{\lambda_{\min}} - \zeta\right)\left(\frac{1}{R} + \frac{1}{\sqrt{\pi D t}}\right). \quad (4)$$

We propose a power-exponential dependency of $\sqrt{\langle h^2\rangle}$ on R, $\sqrt{\langle h^2\rangle} = \sqrt{\langle h_0^2\rangle}(R_0/R)^n$, with initial conditions R_0 and $\sqrt{\langle h_0^2\rangle}$. This form is grounded in MD results that reveal a pronounced inverse relationship between $\sqrt{\langle h^2\rangle}$ and R; a peak in the $\sqrt{\langle h^2\rangle}$ profile aligns a trough in R. n reflects the influence of nanoscale dimensions on interfacial thermal motion ($n \geq 0$). Since $dR/dt \propto R^{2n-2}\ln R$ can be extrapolated from Eq. (4), we suggest that only if $n > 1$, a self-stabilizing effect emerges as $dR/dt \to 0$ when $R \to 0$. This interplay between curvature $1/R$ and reducing γ due to thermal motion acts as a stabilizing force, preventing a surge in Laplace pressure as R diminishes.

To validate Eq. (4), we track the behavior of a sufficiently oscillated dense nanobubble ($N_L = 15$) with an initial $R_0 = 2.64$ nm. Figure 3 illustrates the bubble's dissolution over 100 ns under 1 atm. Two TWC-based models, one with MD simulated $\sqrt{\langle h^2\rangle}$ and another employing $\sqrt{\langle h^2\rangle} = \sqrt{\langle h_0^2\rangle}(R_0/R)^n$, evidence the bubble's size decrease by only 5% in 100 ns, supporting substantial longevity. This result, strongly supported by direct MD simulation, contrasts the EP model's prediction of a rapid 5% shrinkage within 1.5 ns and complete dissolution by 56 ns. Moreover, n, ascertained from the MD-generated $\sqrt{\langle h^2\rangle} - R$ plots [Fig. 3(b)], is determined to be ~2, substantiating the theoretical stability threshold ($n > 1$). This value highlights the dominance of the TCW effect over volumetric changes in maintaining bubble stability. The applicability of Eq. (4) across a wider range of cases, including undersaturation, oversaturation, and varying durations of oscillation, is further demonstrated and showcased in SM.

In expanding our model's purview, we scrutinize bubble stability across scales from nano- to submicron, covering both bulk nanobubbles (typically $R > 50$ nm) [52] and potential cavitation nuclei ($R < 420$ nm) [53]. Figure 3(c) shows a bubble's evolution with $R_0 = 1$ μm and $\zeta = 0.1$, for correlation coefficients $n = 1$ to 3. Employing a conservative estimate for initial $\sqrt{\langle h_0^2\rangle} = 0.287$ nm from Eq. (1), the TCW-EP model anticipates an initial contraction (< 1 s), mirroring classical EP, then rapidly stabilizes at 100–500 nm. The equilibrium radius R_e is given by

$$R_e(n) = \frac{\lambda_{\min}}{\pi}\exp\left(\frac{W(A_n)}{2n-1}\right),$$
$$\text{with} \quad A_n = \frac{(2n-1)\zeta P_\infty\langle h_0^2\rangle(\pi R_0)^{2n}}{k_B T\lambda_{\min}^{2n-1}}, \quad (5)$$

where W represents the Lamber W function, A_n simplifies initial conditions. Figure 3(d) correlates R_e to A_n for $n = 2$, and shows a reasonable range of for A_2's parameters under typical physical conditions ($P_\infty \sim 10^5$ Pa, $T \sim 300$ K, $\zeta \sim 10^{-1}$, $\sqrt{\langle h_0^2\rangle} \sim 0.1$ to 0.3 nm, $R_0 \sim 500$ to 1000 nm). Notably, R_e increases with n, $\sqrt{\langle h_0^2\rangle}$, R_0, and ζ, but, counterintuitively, decreases with T, as suggested by dynamic light scattering studies [54]. Within this rational parameter space, $A_2 \sim 2 \times 10^9$ to 3×10^{10}, placing the predicted R_e values with the experimentally observed nanobubble sizes of 90 to 215 nm [52,55]. Beyond the micrometer-scale threshold, TCW become negligible compared to gravitational and hydrodynamic effects, transitioning our model to macroscopic bubble dynamics.

A further question concerns the persistence of bulk nanobubbles in the face of potential rapid diffusion due to the dense inner gas. We argue that this is strongly correlated with the significantly lower diffusion coefficient within the nanobubbles. Figure 4(a) shows the radial distribution of the oxygen cluster's diffusion coefficient D in a stable bubble ($R = 2.5$ nm) obtained after 100 ns in Fig. 3, revealing an order of magnitude lower D inside the bubble (2.0×10^{-10} m/s^2) compared to the surrounding medium (2.3×10^{-9} m/s^2), with a distinct diffusion boundary layer (1.0×10^{-9} m/s^2 on average). The internal oxygen density ($\rho \propto d^{-3}$, $d \sim 0.5$ nm) reaches 2 orders of magnitude higher than that at atmospheric pressure ($d \sim 3.3$ nm), aligning with our simulations [Fig. 2(c)] and x-ray microscopy data ($d = 0.714$–0.839 nm) [56]. This

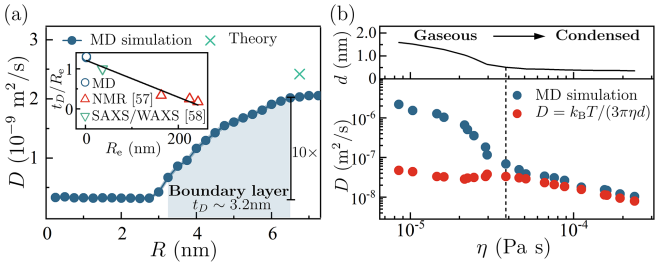

FIG. 4. Diffusion properties of bulk nanobubbles. (a) Radial distribution of the diffusion coefficient D of oxygen in a stable nanobubble solution. The inset shows the relative thicknesses t_D/R_e of the diffusion boundary layer for nanobubbles with different equilibrium radii R_e reported in Ref. [57,58]. (b) D from 20 independent MD systems and calculated from the Stokes-Einstein relation; see SM for simulation method.

suggests a shift from gaseous to condensed state, as evidenced in Fig. 4(b)'s analysis of viscosity η and diffusion coefficients D in 20 independent oxygen systems across varied mean molecular spacing d. We identify a gas-condensed state transition at $d \sim 0.5$ nm, where simulated $D-\eta$ relationship satisfies the Stokes-Einstein equation $D = k_B T/3\pi\eta d$. This echoes previous evidences [Figs. 2(b) and 2(c)], showing a sharp decrease in D and η with the condensed state transition. Another convincing interpretation arises from the notable diffusion boundary layer, validated experimentally. Low field nuclear magnetic resonance analysis reveals a relative thickness of boundary layer t_D/R_e varies from 17% to 34% ($R_e = 242$–163 nm), expanding as bubble size diminishes [57]. Small- and wide-angle x-ray scattering analysis predicts $t_D/R_e = 1$ ($R_e = 37$ nm), attributing this layer's formation to gas adsorption-desorption cycles [58]. Experiments indicate a near-linear t_D/R_e versus R_e correlation [57,58] [inset in Fig. 4(a)], extending to yield a substantial $t_D \sim 3.2$ nm with $R_e \sim 2.5$ nm, corroborating our simulations. This thickening could be ascribed to a "shell effect" [59] wherein nanobubble interface dynamics outpace diffusion equilibrium adjustments under acoustic cavitation, leading to a lag or a slip of boundary layer relative to the liquid phase. In addition, another factor associating t_D with the oscillation's angular frequency, ω, is based on viscous flow theory, with $t_D \sim \sqrt{2\eta/\rho\omega}$ [60].

In conclusion, our model, encouraged by *in situ* SEM characterization, elucidates the remarkable stability of bulk nanobubbles, rooted in a negative feedback loop between TCWs and surface tension. Enhanced TCWs, driven by local densification from gas enrichment and diffusion shielding during acoustic cavitation, play a crucial role. Our theory bridges bubble dynamics across scales through statistical thermodynamics. In real solutions, gas enrichment and nanobubble clustering would be enhanced over larger spatial-temporal scales. The dynamic equilibrium within these clusters, with oscillating local gas concentrations, increases the survival probability of individual nanobubbles, warranting further exploration.

Acknowledgments—We are grateful to Zeiss for discussion on the *in situ* liquid phase SEM experiment and to Dr. Mingbo Li for preparing nanobubble solution. This research was supported by funding from the State Key Program of National Natural Science of China (Grant No. 92252205), and Marine Equipment Foresight Innovation Union Project (No. 2-A3).

[1] A. J. Atkinson, O. G. Apul, O. Schneider, S. Garcia-Segura, and P. Westerhoff, Acc. Chem. Res. **52**, 1196 (2019).
[2] M. R. Ghaani, P. G. Kusalik, and N. J. English, Sci. Adv. **6**, eaaz0094 (2020).
[3] S. R. German, M. A. Edwards, Q. Chen, and H. S. White, Nano Lett. **16**, 6691 (2016).
[4] D. Lohse and X. Zhang, Phys. Rev. E **91**, 031003(R) (2015).
[5] B. H. Tan, H. An, and C.-D. Ohl, Phys. Rev. Lett. **124**, 134503 (2020).
[6] E. D. Michailidi, G. Bomis, A. Varoutoglou, G. Z. Kyzas, G. Mitrikas, A. C. Mitropoulos, E. K. Efthimiadou, and E. P. Favvas, J. Colloid Interface Sci. **564**, 371 (2020).
[7] J. N. Meegoda, S. A. Hewage, and J. H. Batagoda, Langmuir **35**, 12100 (2019).
[8] S. Wang, L. Zhou, and Y. Gao, Phys. Chem. Chem. Phys. **23**, 16501 (2021).
[9] K. Yasui, T. Tuziuti, W. Kanematsu, and K. Kato, Langmuir **32**, 11101 (2016).
[10] C. U. Chan, L. Chen, M. Arora, and C.-D. Ohl, Phys. Rev. Lett. **114**, 114505 (2015).
[11] K. Yasui, T. Tuziuti, and W. Kanematsu, Langmuir **39**, 16574 (2023).
[12] K. Yasui, T. Tuziuti, N. Izu, and W. Kanematsu, Ultrason. Sonochem. **52**, 13 (2019).
[13] K. Ohgaki, N. Q. Khanh, Y. Joden, A. Tsuji, and T. Nakagawa, Chem. Eng. Sci. **65**, 1296 (2010).
[14] J. H. Weijs, J. R. T. Seddon, and D. Lohse, Chem. Phys. Chem. **13**, 2197 (2012).
[15] J. S. Rowlinson and B. Widom, *Molecular Theory of Capillarity* (Dover Publications, Mineola, New York, 2002).
[16] S. Safran, *Statistical Thermodynamics of Surfaces, Interfaces, and Membranes* (CRC Press, Boca Raton, 2019).
[17] D. G. A. L. Aarts, M. Schmidt, and H. N. W. Lekkerkerker, Science **304**, 847 (2004).
[18] D. Derks, D. G. A. L. Aarts, D. Bonn, H. N. W. Lekkerkerker, and A. Imhof, Phys. Rev. Lett. **97**, 038301 (2006).
[19] C. Zhao, Z. Zhang, and T. Si, Phys. Fluids **35**, 072016 (2023).
[20] J. Liu, C. Zhao, D. A. Lockerby, and J. E. Sprittles, Phys. Rev. E **107**, 015105 (2023).
[21] R. Delgado-Buscalioni, E. Chacon, and P. Tarazona, Phys. Rev. Lett. **101**, 106102 (2008).
[22] C. Hernandez, L. Nieves, A. C. de Leon, R. Advincula, and A. A. Exner, ACS Appl. Mater. Interfaces **10**, 9949 (2018).
[23] R. Xiong, R. X. Xu, C. Huang, S. D. Smedt, and K. Braeckmans, Chem. Soc. Rev. **50**, 5746 (2021).
[24] S. Perumanath, M. K. Borg, M. V. Chubynsky, J. E. Sprittles, and J. M. Reese, Phys. Rev. Lett. **122**, 104501 (2019).
[25] M. Moseler and U. Landman, Science **289**, 1165 (2000).

[26] J. Eggers, Phys. Rev. Lett. **89**, 084502 (2002).
[27] See Supplemental Material at http://link.aps.org/supplemental/10.1103/PhysRevLett.133.104001 for (i) *in situ* SEM characterizations, (ii) the MD simulation of nanobubbles, (iii) thermodynamics of nanoscale cavitation, (iv) validation of nanocavity dynamics, and (v) further clarification of nanobubble diffusion behavior, which includes Refs. [28–41]. Readers are also invited to view supplemental movies, including full- motion comparison of pure water and nanobubble solution during SEM imaging and large-scale molecular dynamics simulation of cavitation nucleation. See the LAMMPS script at Ref. [28].
[28] https://github.com/Luwen-Zhang/Nanobubbles.git.
[29] N. Nirmalkar, A. W. Pacek, and M. Barigou, Soft Matter **14**, 9643 (2018).
[30] N. Nirmalkar, A. W. Pacek, and M. Barigou, Langmuir **34**, 10964 (2018).
[31] S. Lloyd, IEEE Trans. Inf. Theory **28**, 129 (1982).
[32] S. Suzuki and K. be, Comput. Vis. Graph. Image Process. **30**, 32 (1985).
[33] A. P. Thompson, H. M. Aktulga, R. Berger, D. S. Bolintineanu, W. M. Brown, P. S. Crozier, P. J. in 't Veld, A. Kohlmeyer, S. G. Moore, T. D. Nguyen, R. Shan, M. J. Stevens, J. Tranchida, C. Trott, and S. J. Plimpton, Comput. Phys. Commun. **271**, 108171 (2022).
[34] R. W. Hockney and J. W. Eastwood, *Computer Simulation Using Particles* (CRC Press, Boca Raton, 1988).
[35] J. L. F. Abascal, M. A. Gonzalez, J. L. Aragones, and C. Valeriani, J. Chem. Phys. **138**, 084508 (2013).
[36] A. P. Thompson, S. J. Plimpton, and W. Mattson, J. Chem. Phys. **131**, 154107 (2009).
[37] L. Costigliola, D. M. Heyes, T. B. Schrøder, and J. C. Dyre, J. Chem. Phys. **150**, 021101 (2019).
[38] J. Green, D. J. Durben, G. H. Wolf, and C. Angell, Science **249**, 649 (1990).
[39] Q. Zheng, D. J. Durben, G. H. Wolf, and C. A. Angell, Science **254**, 829 (1991).
[40] A. D. Alvarenga, M. Grimsditch, and R. J. Bodnar, J. Chem. Phys. **98**, 8392 (1993).
[41] L. Rayleigh, London, Edinburgh, Dublin Philos. Mag. J. Sci. **34**, 94 (1917).
[42] M. S. Plesset and A. Prosperetti, Annu. Rev. Fluid Mech. **9**, 145 (1977).
[43] J. M. Grogan, N. M. Schneider, F. M. Ross, and H. H. Bau, Nano Lett. **14**, 359 (2014).
[44] G. C. Egan, E. Y. Lau, and E. Schwegler, Nano Lett. **22**, 1053 (2022).
[45] J. L. F. Abascal and C. Vega, J. Chem. Phys. **123**, 234505 (2005).
[46] J. Alejandre and G. A. Chapela, J. Chem. Phys. **132**, 014701 (2010).
[47] T. Leong, M. Ashokkumar, and S. Kentish, *Handbook of Ultrasonics and Sonochemistry* (Springer, Singapore, 2016), pp. 69–98.
[48] E. D. Gadea, V. Molinero, and D. A. Scherlis, Nano Lett. **23**, 7206 (2023).
[49] Z. Gao, W. Wu, W. Sun, and B. Wang, Langmuir **37**, 11281 (2021).
[50] E. W. Lemmon, I. H. Bell, M. L. Huber, and M. O. McLinden, Thermophysical Properties of Fluid Systems, in *NIST Chemistry WebBook, NIST Standard Reference Database Number 69* (National Institute of Standards and Technology, Gaithersburg, 2023).
[51] P. S. Epstein and M. S. Plesset, J. Chem. Phys. **18**, 1505 (1950).
[52] G. Ferraro, A. J. Jadhav, and M. Barigou, Nanoscale **12**, 15869 (2020).
[53] J. M. Rosselló and C.-D. Ohl, Phys. Rev. Lett. **127**, 044502 (2021).
[54] M. Li, X. Ma, J. Eisener, P. Pfeiffer, C.-D. Ohl, and C. Sun, J. Colloid Interface Sci. **596**, 184 (2021).
[55] Z. Han, H. Chen, C. He, G. Dodbiba, A. Otsuki, Y. Wei, and T. Fujita, Sci. Rep. **13**, 3663 (2023).
[56] L. Zhou, X. Wang, H.-J. Shin, J. Wang, R. Tai, X. Zhang, H. Fang, W. Xiao, L. Wang, C. Wang, X. Gao, J. Hu, and L. Zhang, J. Am. Chem. Soc. **142**, 5583 (2020).
[57] R. Zhang, Y. Gao, L. Chen, and G. Ge, J. Colloid Interface Sci. **609**, 637 (2022).
[58] M. Hirai, S. Ajito, K. Takahashi, T. Iwasa, X. Li, D. Wen, R. Kawai-Hirai, N. Ohta, N. Igarashi, and N. Shimizu, J. Phys. Chem. B **123**, 3421 (2019).
[59] A. Eller and H. G. Flynn, J. Acoust. Soc. Am. **37**, 493 (1965).
[60] J. Wu and G. Du, J. Acoust. Soc. Am. **101**, 1899 (1997).